

# Modelling of Magnetorheological Fluids with Combined Lattice Boltzmann and Discrete Element Approach

K. Han\*, Y. T. Feng and D. R. J. Owen

*Civil and Computational Engineering Centre, School of Engineering,  
Swansea University, SA2 8PP, UK.*

Received 4 August 2009; Accepted (in revised version) 16 October 2009

Communicated by Boo-Cheong Khoo

Available online 6 January 2010

---

**Abstract.** A combined lattice Boltzmann and discrete element approach is proposed for numerical modelling of magnetorheological fluids. In its formulation, the particle dynamics is simulated by the discrete element method, while the fluid field is resolved with the lattice Boltzmann method. The coupling between the fluid and the particles are realized through the hydrodynamic interactions. Procedures for computing magnetic, contact and hydrodynamic forces are discussed in detail. The applicability of the proposed solution procedure is illustrated via a two-stage simulation of a MR fluid problem with four different particle volume fractions. At the first stage, simulations are performed for the particle chain formation upon application of an external magnetic field; and at the second stage, the rheological properties of the MR fluid under different shear loading conditions are investigated with the particle chains established at the first stage as the initial configuration.

**AMS subject classifications:** 65Z

**Key words:** Magnetorheological fluids, particle dynamics, rheological properties, magnetic interaction models, lattice Boltzmann method, discrete element method.

---

## 1 Introduction

Since the discovery of magnetorheological fluids (MR fluids) by American inventor Jacob Rabinow [23] in the 1940s, the MR technology has found many control-based applications such as dampers, shock absorbers, brakes and clutches in automotive, aerospace and some other industries. A structure based on MR fluids might be the next generation in

---

\*Corresponding author. *Email addresses:* K.Han@swansea.ac.uk (K. Han), y.feng@swansea.ac.uk (Y. T. Feng), d.r.j.owen@swansea.ac.uk (D. R. J. Owen)

design for products where power density, accuracy and dynamic performance are the key features [21].

A MR fluid is a type of smart fluid. It consists of micron-sized magnetizable particles dispersed in a non-magnetic carrier fluid. In the absence of a magnetic field, the rheological behaviour of a MR fluid is basically that of the carrier fluid, except that the suspended magnetizable particles makes the fluid 'thicker'. When subjected to an external magnetic field, the particles become magnetized and acquire a dipole moment. Due to magnetic dipolar interactions, the particles line up and form chainlike structures in the direction of the applied field. This change in the suspension microstructure significantly alters the rheological properties of the fluid. The viscosity of the fluid is increased as the fluid motion is largely restricted by the particle chains. Also the yield stress of the fluid increases with the applied magnetic field strength and can be controlled very accurately. Besides, the response of the MR fluid to the applied magnetic field is usually rapid (in milliseconds). The MR effect is also reversible. When the magnetic field is removed, the original condition of the fluid is re-established [21].

Experimental and theoretical studies have been reported to better understand and predict the behaviour of MR fluids. Particularly from the design prospective it is important to establish the quantitative relationship between the rheological properties (viscosity, yield stress etc) and the volume concentration fraction of the particles and their magnetic properties as well as the intensity of the applied magnetic field. Due to the limitations in the experiments and over-simplifications in the theoretical analysis, numerical modelling has become increasingly important in recent years as a powerful prediction tool for modelling the rheological behavior of MR fluids.

For instance, Ly *et al.* [19] performed two-dimensional particle dynamics simulations of MR fluids, where the motion of the particles was governed by magnetic, hydrodynamic, and repulsive interactions; fluid-particle interactions were accounted for via Stokes' drag while inter-particle repulsions were modelled through approximate hard-sphere rejections; magnetostatic forces were derived from the solution of (steady) Maxwell's equations by employing a fast multipole method on a boundary integral formulation. Kang *et al.* [14] recently developed a direct numerical simulation method based on the Maxwell stress tensor and a fictitious domain method. Particles were assumed to be non-Brownian with negligible inertia. Rigid body motions of particles in two-dimensions were described by a rigid-ring description implemented by Lagrange multipliers. The magnetic force was represented by the divergence of the Maxwell stress tensor, which acted as a body force added to the momentum balance equation. Keaveny *et al.* [15] developed a new model to accelerate the calculation of many-body dipole interactions, where each particle's magnetization was represented as a finite distribution of current density. The exact solution to the two-body problem was also presented and a technique was introduced to blend this result with a many-body dipole calculation.

Numerical simulations of MR fluids require an accurate and computationally efficient approach to fully account for magnetic, hydrodynamic and contact interactions. Firstly, the scheme to be employed should be able to effectively model contact phenomena be-

tween the magnetizable particles during the evolution of the magnetic microstructure. It is obviously impractical using a continuum representation (such as finite element) of a large number of individual particles. The discrete element method, among other discontinuous methodologies such as discontinuous deformation analysis and the manifold method, has been successfully employed for modelling problems of a discrete or discontinuous nature. Originated in geotechnical and granular flow applications [6] in the late 70s, the discrete element method is based on the concept that individual material elements are considered to be separate and are connected only along their boundaries by appropriate physically based interaction laws. The motion of the discrete elements is governed by the contact forces and the entire system is evolved by employing an explicit time integration scheme.

Secondly, fluid-particle interaction problems are computationally challenging. With traditional computational fluid dynamics methods, the fluid domain around the particles need to be continuously re-meshed as the particles move across the computational grids. Also sufficient resolution of the particle domain is required. A relatively new numerical technique, the lattice Boltzmann method, overcomes the limitations of the conventional methods by using a fixed, non-adaptive (Eulerian) mesh to represent the flow field. In particular, the moving boundary conditions can be relatively easily implemented in its framework. Since Ladd's pioneer work [18], the lattice Boltzmann method has been extensively employed in modelling fluid-particle interaction problems. A rich publication in recent years (see for instance, [1,5,7,8,11,13,22] and the references therein) has proved the effectiveness of the method.

This work proposes a combined lattice Boltzmann and discrete element approach for modelling MR fluids, in which the particle dynamics is simulated by the discrete element method, while the fluid field is resolved with the lattice Boltzmann method. The coupling between the fluid and the particles are realized through the hydrodynamic interactions. The applicability of the proposed solution procedure is illustrated via a two-stage simulation of a MR fluid with four different particle volume fractions. At the first stage, simulations are performed for the particle chain formation upon application of an external magnetic field; and at the second stage, the rheological properties of the MR fluid under different shear loading conditions are investigated with the particle chains established at the first stage as the initial configuration.

It should be pointed out that the primary objective of the present work is to establish a computational framework for investigating MR fluids at the microscopic level rather than the macroscopic (application) level. Thus a representative volume element (RVE), taken from a large volume MR fluid, is modelled with appropriate boundary conditions imposed. It is also assumed that mono-sized spherical particles are suspended in a Newtonian fluid, and both Brownian and gravitational forces are ignored. To illustrate the solution procedure to be presented, only a monolayer of the fluid is taken which makes it possible to employ a two-dimensional lattice Boltzmann formulation for the fluid field. Because of this simplification, the results obtained from the numerical experiments do not represent the true physical values of a realistic MR fluid, but should give some rea-

sonable indications of the major physical features of the fluid.

In what follows, the discrete element procedure for modelling particle dynamics and the lattice Boltzmann formulation for simulating the fluid field will be discussed in the next two sections with special attention given to the evaluations of the contact, magnetic and hydrodynamic forces. Then the coupling of the governing equations for particles and fluid, as well as the solution algorithm will be presented, followed by numerical examples and conclusion.

## 2 Particle dynamics: The discrete element approach

During the microstructure evolution of a MR fluid subjected to an applied magnetic field, the motion of the magnetized particles is collectively driven by the magnetic, hydrodynamic and contact forces. The classical discrete element method is extended to include all these forces.

In the discrete element formulation, each particle in a MR fluid is treated as a discrete element that interacts with other particles (discrete element) through boundary contact. The particles are assumed rigid, but a small overlap between contacting particles is allowed to generate mechanical contact forces that prevent them from penetrating each other. At each time step, particles in contact are identified with a contact search algorithm; then their interaction forces are evaluated based on appropriate interaction laws. The motion of particles is governed by Newton's second law. A set of governing equations is built up and integrated with respect to time, to update each particle's position, velocity and acceleration. The main building blocks of the discrete element procedure are described as follows.

### 2.1 Governing equations

The motion of the particles is governed by Newton's second law of motion as

$$\mathbf{M}\ddot{\mathbf{u}} + \mathbf{C}_d\dot{\mathbf{u}} = \mathbf{F}_m + \mathbf{F}_f + \mathbf{F}_c, \quad (2.1)$$

where  $\mathbf{M}$  and  $\mathbf{C}_d$  are respectively the mass and damping matrices of the system; and  $\mathbf{u}$ ,  $\dot{\mathbf{u}}$  and  $\ddot{\mathbf{u}}$  are respectively the displacement, velocity and acceleration vectors;  $\mathbf{F}_m$ ,  $\mathbf{F}_f$  and  $\mathbf{F}_c$  denote the magnetic, hydrodynamic and contact forces, respectively.

Note that the computation of the hydrodynamic forces will be discussed in the next section with the lattice Boltzmann method, while the evaluations of the contact and magnetic forces are given in this section.

### 2.2 Time integration

Eq. (2.1) is integrated by employing an explicit time integration scheme. With this scheme, no global stiffness matrix needs to be formed and inverted, which makes the operations at each time step far less computationally intensive.

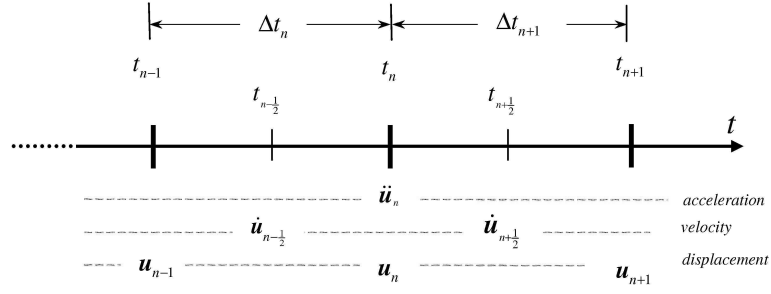


Figure 1: Central difference integration scheme.

Among the explicit schemes, the central difference method is very popular for dynamics and impact since it is a single step scheme and offers a second order accuracy. The procedure is outlined as follows.

A combination of previous and current midpoint velocities,  $\dot{\mathbf{u}}_{n-\frac{1}{2}}$  and  $\dot{\mathbf{u}}_{n+\frac{1}{2}}$ , as illustrated in Fig. 1, forms the second order difference equation that defines the acceleration at time  $t_n$  as

$$\ddot{\mathbf{u}}_n = \ddot{\mathbf{u}}(t_n) = \frac{\dot{\mathbf{u}}_{n+\frac{1}{2}} - \dot{\mathbf{u}}_{n-\frac{1}{2}}}{\Delta t_{n+\frac{1}{2}}}. \tag{2.2}$$

Through the direct integration of the acceleration term with respect to the time increment, the velocity at time  $t_n$  can be approximated as

$$\dot{\mathbf{u}}_n = \dot{\mathbf{u}}(t_n) = \frac{\mathbf{u}_{n+\frac{1}{2}} - \mathbf{u}_{n-\frac{1}{2}}}{\Delta t_{n+\frac{1}{2}}} = \frac{\mathbf{u}_{n+1} - \mathbf{u}_{n-1}}{2\Delta t_{n+\frac{1}{2}}} = \frac{\Delta t_{n+1}\dot{\mathbf{u}}_{n+\frac{1}{2}} + \Delta t_n\dot{\mathbf{u}}_{n-\frac{1}{2}}}{2\Delta t_{n+\frac{1}{2}}}, \tag{2.3}$$

where the midpoint velocities are defined as

$$\dot{\mathbf{u}}_{n-\frac{1}{2}} = \dot{\mathbf{u}}(t_{n-\frac{1}{2}}) = \frac{\mathbf{u}_n - \mathbf{u}_{n-1}}{\Delta t_n}, \quad \dot{\mathbf{u}}_{n+\frac{1}{2}} = \dot{\mathbf{u}}(t_{n+\frac{1}{2}}) = \frac{\mathbf{u}_{n+1} - \mathbf{u}_n}{\Delta t_{n+1}} \tag{2.4}$$

and the time increments are calculated as

$$\Delta t_n = t_n - t_{n-1}, \quad \Delta t_{n+1} = t_{n+1} - t_n, \quad \Delta t_{n+\frac{1}{2}} = \frac{1}{2}(\Delta t_n + \Delta t_{n+1}). \tag{2.5}$$

By substituting Eqs. (2.2) and (2.3) into (2.1) the velocity at time  $t_{n+\frac{1}{2}}$  is determined in terms of known (previous) velocity, displacement and force quantities,

$$\dot{\mathbf{u}}_{n+\frac{1}{2}} = \dot{\mathbf{u}}(t_{n+\frac{1}{2}}) = \left[ 2\mathbf{M} + \mathbf{C}_d\Delta t_{n+1} \right]^{-1} \left[ (2\mathbf{M} - \mathbf{C}_d\Delta t_n)\dot{\mathbf{u}}_{n-\frac{1}{2}} + 2\Delta t_{n+\frac{1}{2}}\mathbf{F} \right], \tag{2.6}$$

where  $\mathbf{F}$  denotes the force terms on the right hand side of Eq. (2.1). Thus the displacement at time  $t_{n+1}$  can be calculated as

$$\mathbf{u}_{n+1} = \mathbf{u}(t_{n+1}) = \mathbf{u}_n + \dot{\mathbf{u}}_{n+\frac{1}{2}}\Delta t_{n+1} \tag{2.7}$$

and the force vector is updated by

$$\mathbf{F}_{n+1} = \mathbf{F}(t_{n+1}). \quad (2.8)$$

Since displacements and velocities are computed at different time instances in the central difference algorithm, a starting scheme is required to provide an initial value for velocity at  $t = \frac{1}{2}\Delta t_1$ . The following procedure is used to compute  $\dot{\mathbf{u}}_{\frac{1}{2}}$  in this work:

$$\dot{\mathbf{u}}_{\frac{1}{2}} = \mathbf{u}_0 + \mathbf{M}^{-1}(\mathbf{F} - \mathbf{C}_d \dot{\mathbf{u}}_0) \frac{\Delta t_1}{2}, \quad (2.9)$$

where  $\mathbf{u}_0$  and  $\dot{\mathbf{u}}_0$  are the initial displacements and velocities respectively.

However, any explicit time integration scheme is only conditionally stable. If the time increment is too large, the errors are magnified, resulting an unstable solution. In order to maintain a stable solution, the time step has to be smaller than a critical value, which is related to the maximum eigenvalue of the governing equations. For a linear system the critical time step can be evaluated as [2]

$$\Delta t_{cr} = \frac{2}{\omega_{max}}, \quad (2.10)$$

where  $\omega_{max}$  is the maximum eigenvalue of the system. The above result may not be valid for an impact system as it is generally nonlinear, which has been demonstrated in [10]. To ensure a stable and reasonably accurate solution, the critical time step should be no larger than 0.1 times the value given by Eq. (2.10).

### 2.3 Contact search

As the system configuration keeps changing during the course of evolutions, a contact search needs to be performed constantly to build a list of all possible contacts. Since a significant percentage of the total computational effort of a discrete element solution may be associated with this task, a robust and efficient contact detection algorithm is essentially required.

Some search algorithms used in general computing technology and computer graphics have been employed for this purpose. For the detection of potential contact between a large number of discrete elements, a spatial search algorithm based on space-cell subdivision and incorporating a tree data storage structure possesses significant computational advantages. For instance, the augmented spatial digital tree [9], which will be adopted in this work, is a spatial binary tree based contact detection algorithm. It uses the lower corner vertex to represent a rectangle in a binary spatial tree, with the upper corner vertex serving as the augmented information. Numerical experiments in [9] indicate that the augmented spatial digital tree algorithm can reduce the CPU requirement of contact detection from an originally demanding level down to a more acceptable proportion of the computing time.

## 2.4 Contact forces

The contact forces between the contacting particles provide a barrier for inter-particle penetrations, which are evaluated from a physically based interaction law that describes the relationship between the contact overlap or penetration,  $\delta$ , and the corresponding repulsive force,  $F_c$ ,

$$F_c = F(\delta). \quad (2.11)$$

Different assumptions regarding the contact force will result in different contact models. A comprehensive study of the contact interaction laws can be found in [12]. In this work, a penalty method based on Hertzian contact theory is adopted, in which the contact displacement constraints are only approximately satisfied for finite values of the penalty coefficients, allowing a small amount of overlap to occur in the contact zone. The normal contact force,  $F_c$ , is assumed to act along the direction connecting the particles' centres and its magnitude can be computed in terms of the relative approach of two particles as

$$F_c = k_n \delta^{\frac{3}{2}} \quad (2.12)$$

with the penalty coefficient

$$k_n = \frac{4E^* \sqrt{R^*}}{3}, \quad (2.13)$$

where  $R^*$  is the relative radius defined by

$$\frac{1}{R^*} = \frac{1}{R_1} + \frac{1}{R_2}$$

with  $R_1$  and  $R_2$  being the radii of the two particles; and  $E^*$  is the relative Young's modulus related to the elastic properties  $E_1, E_2$ , and  $\nu_1, \nu_2$  of the two particles, given by the following expression

$$\frac{1}{E^*} = \frac{1-\nu_1^2}{E_1} + \frac{1-\nu_2^2}{E_2}.$$

## 2.5 Magnetic forces

The magnetic interaction in a MR fluid can be treated as a magnetostatic problem, which is described by Laplace's equation subject to appropriate boundary conditions. The magnetic forces are resolved by formulating the Maxwell stress tensor from the resultant field. The solution procedure is outlined below, based on [15].

Let  $\mathbf{H}$  and  $\mathbf{B}$  denote the magnetic field intensity and flux density, respectively. For a linear isotropic medium with the magnetic permeability  $\mu$ ,  $\mathbf{H}$  and  $\mathbf{B}$  are related by the constitutive equation

$$\mathbf{B} = \mu \mathbf{H}. \quad (2.14)$$

Assume that the external magnetic field  $\mathbf{H}_0$  is applied along the  $z$  direction with a magnitude  $H_0$ , i.e.  $\mathbf{H}_0 = H_0 \mathbf{z}$ , where  $\mathbf{z}$  denotes the unit vector of the  $z$ -axis. If  $\mu_p$  and  $\mu_f$

represent, respectively, the magnetic permeability of the particles and fluid, then the relative susceptibility,  $\chi$ , and effective susceptibility,  $\chi_e$ , of the particles are defined as

$$\chi = \frac{\mu_p}{\mu_f}, \quad \chi_e = \frac{3(\chi-1)}{\chi+2}.$$

### 2.5.1 Fixed dipole model

When an external magnetic field is applied, each particle in a MR fluid is magnetized and acquires a magnetic dipole moment  $\mathbf{m}$  which, when ignoring the presence of the other particles, is

$$\mathbf{m} = \frac{4\pi R^3}{3} \frac{3(\chi-1)}{\chi+2} \mathbf{H}_0 = C_p \mathbf{H}_0; \quad m = |\mathbf{m}| = C_p H_0, \quad (2.15)$$

where  $C_p = V_p \chi_e$ ;  $V_p = 4\pi R^3/3$  is the volume of the particle.

Consider one particle with dipole moment  $\mathbf{m}_1 = \mathbf{m}$ . The magnetic field produced by this dipole at any point (with a relative position vector  $\mathbf{r}$  to the dipole) in space can be expressed as [24]

$$\mathbf{H}_1(\mathbf{m}_1, \mathbf{r}) = \frac{1}{4\pi} \frac{3(\mathbf{m}_1 \cdot \hat{\mathbf{r}})\hat{\mathbf{r}} - \mathbf{m}_1}{r^3}, \quad (2.16)$$

where  $r = |\mathbf{r}|$  and  $\hat{\mathbf{r}} = \mathbf{r}/r$  is the unit vector of  $\mathbf{r}$ . The corresponding flux density  $\mathbf{B}$  is calculated as

$$\mathbf{B}_1(\mathbf{r}) = \mu \mathbf{H}_1(\mathbf{r}). \quad (2.17)$$

If a second particle of magnetic moment  $\mathbf{m}_2 = \mathbf{m}$  is placed in the magnetic field of  $\mathbf{m}_1$  as illustrated in Fig. 2, the magnetic force,  $\mathbf{F}_m$ , acting on the second dipole due to the first one can be determined by

$$\mathbf{F}_m(\mathbf{r}) = \nabla(\mathbf{m}_2 \cdot \mathbf{B}_1(\mathbf{r})) \quad (2.18)$$

with  $\mathbf{r} = \mathbf{x}_2 - \mathbf{x}_1$ . This force can be expressed more conveniently in a spherical coordinate system  $(r, \theta, \varphi)$  with  $\theta$  and  $\varphi$  being the zenith and azimuth angles, respectively. Particularly, the component of the force in the azimuth angle  $\varphi$  is zero, and the radial and transversal components,  $F_n$  and  $F_\tau$ , can be computed as

$$F_n(r, \theta) = -\frac{3\mu}{4\pi} \frac{m_1 m_2}{r^4} [3\cos^2\theta - 1] = -\frac{3\mu}{4\pi} \frac{m_1 m_2}{r^4} \frac{1}{2} [3\cos 2\theta + 1] \quad (2.19)$$

and

$$F_\tau(r, \theta) = -\frac{3\mu}{4\pi} \frac{m_1 m_2}{r^4} \sin 2\theta. \quad (2.20)$$

Depending on the angle  $\theta$ , the normal component  $F_n$  can be attractive (when  $\theta < \theta_c$ ) or repulsive (when  $\theta > \theta_c$ ), where the critical angle  $\theta_c = 54.47^\circ$ .

Eqs. (2.19) and (2.20) define the magnetic interaction between any two magnetized particles, which is basically the classic magnetic dipole model, or the fixed dipole model. Owing to its simplicity, this model has been commonly used in modelling MR-fluids,

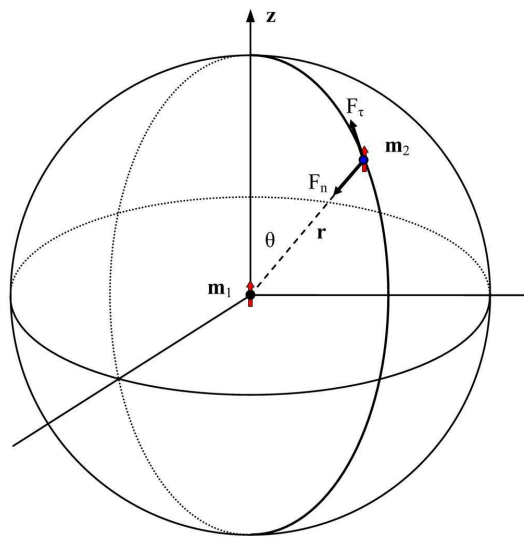


Figure 2: Magnetic forces on dipole moment  $\mathbf{m}_2$  from dipole moment  $\mathbf{m}_1$ .

especially when a large number of particles are involved. The pairwise nature of the model also makes it suitable for use within the discrete element modelling framework.

This fixed dipole model is accurate if the separation distance (gap) of two magnetized particles is larger than their diameter  $2R$  [15], which suggests a cut-off distance to be used in the later magnetic interaction computation,

$$r_c = 4R. \quad (2.21)$$

However, a large error will be introduced when the separation distance between two particles is less than their radius,  $r < R$ . This error arises mainly from the strong interaction between the two magnetized fields of the particles, and will reach maximum when the particles touch each other. The numerical investigation performed in [15] shows that for  $\chi = 5$ , the fixed dipole model underestimates the maximum attraction force by around 35%, while overestimates the maximum repulsive force by 50% or more. The error will become more pronounced for larger susceptibility values.

### 2.5.2 Mutual dipole model

The fixed dipole model discussed above assumes no interactions between the particles' magnetized fields. In fact, the presence of other magnetized particles will increase the magnetization of a particle, thereby enhancing its dipole strength and its interactions with other particles.

If the mutual magnetization between the particles are taken into account, the accuracy of the fixed dipole model may be improved. More specifically, each particle is still viewed

as a point dipole but is subjected to an additional secondary magnetization from the other particles' magnetized fields. Note that the magnetization due to the external field is termed the primary magnetization and the magnetization by other particles' magnetized fields is termed the secondary magnetization.

The mutually magnetized moment of particle  $i$ ,  $\mathbf{m}_i$ , can be evaluated as

$$\mathbf{m}_i = C_p [\mathbf{H}_0 + \mathbf{H}(\mathbf{x}_i)] \quad (i = 1, \dots, N), \quad (2.22)$$

where  $N$  is the total number of particles in the system, and  $\mathbf{H}(\mathbf{x}_i)$  is the total secondary magnetic field generated by all the other magnetized particles at the centre of particle  $i$ ,

$$\mathbf{H}(\mathbf{x}_i) = \sum_{j=1, j \neq i}^N \mathbf{H}_j(\mathbf{m}_j, \mathbf{r}_{ij}) = \sum_{j=1, j \neq i}^N \frac{1}{4\pi} \frac{3\hat{\mathbf{r}}_{ij}(\mathbf{m}_j \cdot \hat{\mathbf{r}}_{ij}) - \mathbf{m}_j}{r_{ij}^3} \quad (2.23)$$

with  $\mathbf{r}_{ij} = \mathbf{x}_i - \mathbf{x}_j$ ;  $r_{ij} = |\mathbf{r}_{ij}|$ ;  $\hat{\mathbf{r}}_{ij} = \mathbf{r}_{ij}/r_{ij}$ .

Eqs. (2.22) and (2.23) define a  $3N \times 3N$  linear system of equations with  $\mathbf{m}_i$  unknown variables. After all the magnetic moments are solved, the magnetic forces between the particles can be determined by the fixed dipole model using these total magnetization moments. This is the idea behind the so-called mutual dipole model [15].

Nevertheless, the computational cost associated with the solution of the linear system of equation (2.23) for systems involving a large number of particles can be substantial, and in particular, the solution needs to be performed at every time step of the simulation. In the present work, the classic Gauss-Seidel algorithm is employed to iteratively solve the equations.

Let  $\mathbf{m}_i^k$  be the approximate values at the  $k$ th iteration, and  $\mathbf{m}_i^0$  be a given initial values. Then at the  $k+1$  iteration  $\mathbf{m}_i$  is computed as

$$\mathbf{m}_i^{k+1} = C_p \left[ \mathbf{H}_0 + \sum_{j=1}^{i-1} \mathbf{H}_j(\mathbf{m}_j^{k+1}, \mathbf{r}_{ij}) + \sum_{j=i+1}^N \mathbf{H}_j(\mathbf{m}_j^k, \mathbf{r}_{ij}) \right]; \quad k = 0, 1, 2, \dots, \quad (2.24)$$

where  $\mathbf{m}_i$  at the previous step serves as the initial value for the current step. As the time step is usually very small, it is a very good initial value and thus the convergence of the iterative scheme is rapid. The numerical tests conducted have shown that the above scheme is very effective, and a solution accuracy of  $10^{-5}$  can be generally achieved in no more than three iterations.

Our numerical investigations show that using this mutual dipole model for two particles in contact, the upper limit of the maximum increased magnetic moment is 33.33% for a perfectly magnetized material ( $\chi = \infty$ ), which gives a 77.78% increase of the attraction force; while the upper limit of the maximum decreased magnetic moment is 11.11% which results in a 20.99% decrease of the repulsive force. The effect is even more significant for a longer chain of particles.

However, as shown in [15], the exact maximum force between two particles in contact is larger than that predicted by the mutual dipole model. Particularly, it is infinite when  $\chi = \infty$ .

Further improvement to the mutual dipole model has been undertaken in [15], in which after the total magnetized moments are obtained, the force between any two particles is calculated by using the two-body exact solution, a special case of the general solution to multiple particle problems [4]. Although some improvement is achieved, the exact solution is still not obtained since the two-body solution is not exact in general multiple particle cases. More importantly, from a computational point of view, this version of the mutual dipole model loses its original simplicity as a result of the substantial computational cost involved in the incorporation of the two-body exact solution.

In view of the difficulties discussed above, a better approach, as proposed in [17], for improving the accuracy but retaining the computational simplicity of the fixed or mutual dipole model is to use some empirical formulae to describe the magnetic interaction when the particles are close to each other. However, the procedure involves substantial pre-computations for different susceptibility values and different relative positions between two particles.

### 3 Hydrodynamics: The lattice Boltzmann approach

The fluid field and the hydrodynamic forces of a MR fluid will be fully resolved with the lattice Boltzmann method.

#### 3.1 Lattice Boltzmann formulation for incompressible fluid flow

Originated from the lattice gas automata method, the lattice Boltzmann method is a 'micro-particle' based numerical time-stepping procedure for the solution of incompressible fluid flows. Instead of solving the Navier-Stokes equations numerically as do the traditional computational fluid dynamics methods, the lattice Boltzmann method simulates fluid flows by tracking the evolution of fluid particle density distributions. Once the density distribution function is solved, the macroscopic variables of the fluid field can be conveniently calculated from its first two hydrodynamic moments.

In the lattice Boltzmann method, space is divided into square lattice nodes. The fluid is modeled as a group of fluid particles that are allowed to move between lattice nodes or stay at rest. During each discrete time step of the simulation, fluid particles move to the nearest lattice node along their directions of motion, where they 'collide' with other fluid particles that arrive at the same node. The outcome of the collision is determined by solving the kinetic (Boltzmann) equation for the new distribution function at that node and the fluid particle distribution function is updated [3].

The evolution of the density distribution functions at each time step is given by the following lattice Boltzmann equation

$$f_i(\mathbf{x} + \mathbf{e}_i \Delta t, t + \Delta t) - f_i(\mathbf{x}, t) = -\frac{1}{\tau} [f_i(\mathbf{x}, t) - f_i^{eq}(\mathbf{x}, t)], \quad (3.1)$$

where for any grid node  $\mathbf{x}$ ,  $\mathbf{x} + \mathbf{e}_i \Delta t$  is its nearest node along direction  $i$ ;  $f_i$  denotes the fluid particle density distribution function, each relating the probable amount of fluid particles moving with the velocity  $\mathbf{e}_i$  along the  $i$ -th direction at each node. In the widely used two-dimensional nine-speed (D2Q9) model,  $\mathbf{e}_i$  is defined as

$$\begin{cases} \mathbf{e}_0 = (0,0), \\ \mathbf{e}_i = c \left[ \cos \frac{\pi(i-1)}{2}, \sin \frac{\pi(i-1)}{2} \right] & (i=1, \dots, 4), \\ \mathbf{e}_i = c \left[ \cos \frac{\pi(2i-9)}{4}, \sin \frac{\pi(2i-9)}{4} \right] & (i=5, \dots, 8), \end{cases} \quad (3.2)$$

in which  $c$  is termed the lattice speed and given by

$$c = h / \Delta t$$

with  $h$  the lattice spacing and  $\Delta t$  the discrete time step.

The collision operator on the right-hand side of Eq. (3.1) is used to redistribute the fluid particle density  $f_i$  towards its local equilibrium  $f_i^{eq}$ ; and the rate of approach to equilibrium is controlled by the relaxation time parameter  $\tau$ . The equilibrium distribution function  $f_i^{eq}$  is given in the D2Q9 model as

$$\begin{cases} f_0^{eq} = \rho \left[ 1 - \frac{3}{2c^2} \mathbf{v} \cdot \mathbf{v} \right], \\ f_i^{eq} = w_i \rho \left[ 1 + \frac{3}{c^2} \mathbf{e}_i \cdot \mathbf{v} + \frac{9}{2c^4} (\mathbf{e}_i \cdot \mathbf{v})^2 - \frac{3}{2c^2} \mathbf{v} \cdot \mathbf{v} \right] & (i=1, \dots, 8), \end{cases} \quad (3.3)$$

with

$$w_0 = \frac{4}{9}; \quad w_{1-4} = \frac{1}{9}; \quad w_{5-8} = \frac{1}{36}. \quad (3.4)$$

The lattice Boltzmann equation (3.1) is explicitly solved in the following two steps: 1) collision towards local equilibrium through relaxation:

$$f_i^+(\mathbf{x}, t) = f_i(\mathbf{x}, t) - \frac{1}{\tau} [f_i(\mathbf{x}, t) - f_i^{eq}(\mathbf{x}, t)] \quad (3.5)$$

and 2) propagation to the nearest lattice node:

$$f_i(\mathbf{x} + \mathbf{e}_i \Delta t, t + \Delta t) = f_i^+(\mathbf{x}, t). \quad (3.6)$$

The macroscopic density  $\rho$  and velocity  $\mathbf{v}$  of the flow field are computed from

$$\rho = \sum_{i=0}^8 f_i, \quad \rho \mathbf{v} = \sum_{i=1}^8 f_i \mathbf{e}_i. \quad (3.7)$$

The pressure field  $p$  can be obtained through a simple equation of state

$$p = c_s^2 \rho, \quad (3.8)$$

where  $c_s$  denotes the fluid speed of sound and is related to the lattice speed  $c$  by

$$c_s = c / \sqrt{3}. \quad (3.9)$$

The kinematic viscosity of the fluid is related to other model parameters as

$$\nu_f = \frac{1}{3} \left( \tau - \frac{1}{2} \right) \frac{h^2}{\Delta t} = \frac{1}{3} \left( \tau - \frac{1}{2} \right) ch. \quad (3.10)$$

It is worth pointing out that the Chapman-Enskog expansion for the density distribution function can recover the continuity and Navier-Stokes equations in the incompressible limit. Therefore the computational Mach number should be sufficiently small to ensure a reasonably accurate solution. Other computational issues can be found in [11].

### 3.2 Hydrodynamic forces

To compute the hydrodynamic forces acting on a moving particle in the fluid, the collision operator in the lattice Boltzmann equation (3.1) needs to be modified so that it shifts smoothly between hydrodynamics at nodes occupied solely by fluid and rigid body motion at nodes occupied solely by particles.

Ladd [18] proposes a modification to the bounce-back rule so that the movement of a solid particle can be accommodated. This approach provides a relationship of the exchange of momentum between the fluid and the solid boundary nodes. It also assumes that the fluid fills the entire volume of the solid particle, or in other words, the particle is modeled as a 'shell' filled with fluid. As a result, both solid and fluid nodes on either side of the boundary surface are treated in an identical fashion. It has been observed, however, that the computed hydrodynamic forces may suffer from severe fluctuations when the particle moves across the grid with a large velocity. This is mainly caused by the step-wise representation of the solid particle boundary and the constant changing boundary configurations.

To circumvent the fluctuation of the computed hydrodynamic forces with the modified bounce-back rule, Noble and Torczynski [20] proposed an immersed moving boundary technique. In this approach, the fluid and solid volume fractions are used to weigh the corresponding portions of the collision term for nodes with both phases present. By introducing additional collision terms that account for the interactions with each solid obstacle within the computational cell, the evolution equation then becomes

$$f_i(\mathbf{x} + \mathbf{e}_i \Delta t, t + \Delta t) = f_i(\mathbf{x}, t) - \frac{1}{\tau} (1 - \beta) [f_i(\mathbf{x}, t) - f_i^{eq}] + \beta f_i^m, \quad (3.11)$$

where  $\beta$  is a weighting function depending on the local fluid/solid ratio  $\gamma$ ; and  $f_i^m$  is an additional term computed by

$$\begin{cases} \beta = \frac{\gamma(\tau - 0.5)}{(1 - \gamma) + (\tau - 0.5)}, \\ f_i^m = f_{-i}(\mathbf{x}, t) - f_i(\mathbf{x}, t) + f_i^{eq}(\rho, \mathbf{v}_b) - f_{-i}^{eq}(\rho, \mathbf{v}), \end{cases} \quad (3.12)$$

where  $\mathbf{v}_b$  is the velocity of the particle. Then the hydrodynamic forces exerted on a solid particle over  $n$  particle-covered nodes are summed up as

$$\mathbf{F}_f = 2Rch \left[ \sum_n \left( \beta_n \sum_i f_i^m \mathbf{e}_i \right) \right], \quad (3.13)$$

where  $\mathbf{x}_n$  is the coordinate of the lattice node  $n$ .

With this approach, the computed hydrodynamic forces are sufficiently smooth, which is also confirmed by our previous numerical tests [11, 13].

Note that a spherical particle can only be treated as a cylinder in the above computation and the factor  $2R$  on the right hand side takes into account the third dimension of the particle. Clearly the computed hydrodynamic force is for a cylinder rather than a sphere and some discrepancy will arise. This is the main source of error in the current quasi-3D model.

## 4 Coupling between particle dynamics and hydrodynamics

The fluid field is governed by the lattice Boltzmann equation (3.1) and evolves in an explicit manner. The dynamic equations of the particles are governed by Eq. (2.1) and solved by the central difference algorithm. The coupling between the fluid and the particles are realized through the hydrodynamic interactions.

There are two time steps used in the combined lattice Boltzmann and discrete element procedure,  $\Delta t$  for the fluid flow and  $\Delta t_D$  for the particles. Since  $\Delta t_D$  is generally smaller than  $\Delta t$ , it has to be reduced to  $\Delta t_s$  so that the ratio between  $\Delta t$  and  $\Delta t_s$  is an integer  $n_s$ ,

$$\Delta t_s = \frac{\Delta t}{n_s} \quad (n_s = \lceil \Delta t / \Delta t_D \rceil + 1), \quad (4.1)$$

where  $\lceil \cdot \rceil$  denotes an integer round-off operator. This gives rise to a so-called subcycling time integration for the discrete element part; in one step of the fluid computation,  $n_s$  sub-steps of integration are performed for Eq. (2.1) using the time step  $\Delta t_s$ , whilst the hydrodynamic forces  $\mathbf{F}_f$  are kept unchanged during the subcycling.

Since the lattice Boltzmann equation is implemented in the lattice coordinate system in this work, the dynamic equation Eq. (2.1) for the particles should be implemented in the same way. It can be derived that in the lattice coordinate system Eq. (2.1) takes the form of

$$\bar{\mathbf{M}}\bar{\mathbf{u}} + \bar{\mathbf{C}}_d\bar{\mathbf{u}} = \bar{\mathbf{F}}_m + \bar{\mathbf{F}}_f + \bar{\mathbf{F}}_c, \quad (4.2)$$

where

$$\begin{cases} \bar{\mathbf{M}} = \mathbf{M}/h^3; & \bar{\mathbf{u}} = \mathbf{u}/c, \\ \bar{\mathbf{u}} = \mathbf{u}\Delta t/c; & \bar{\mathbf{C}}_d = \mathbf{C}_dch, \\ \bar{\mathbf{F}}_m = \mathbf{F}_m/c^2; & \bar{\mathbf{F}}_f = \mathbf{F}_f/(c^2h), \\ \bar{\mathbf{F}}_c = \mathbf{F}_c/c^2. \end{cases}$$

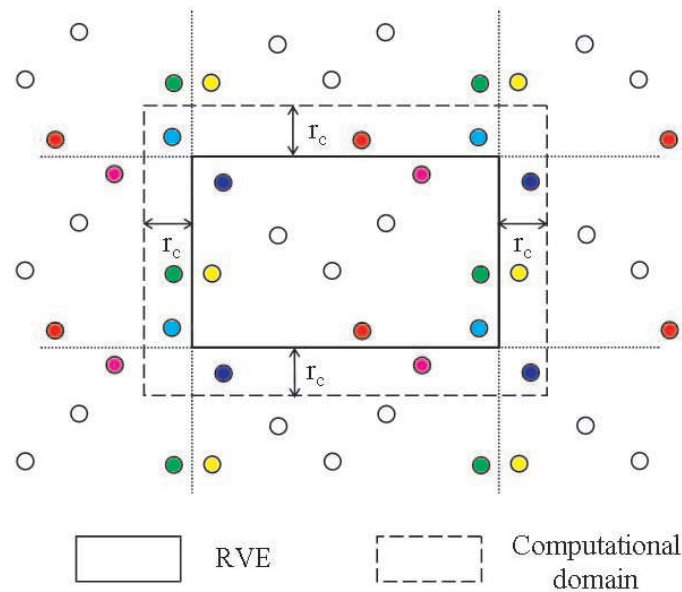


Figure 3: A RVE and computational domain; particles with their counterparts in image cells.

## 5 Representative volume element and periodic boundary conditions

As mentioned earlier, the present work aims at investigating the general behaviour of MR fluids without considering specific operational/application conditions. Therefore a representative volume element (RVE) of a MR fluid is modelled, whose behaviour should provide a general indication of the problem concerned.

The RVE is a region taken from a MR fluid parallel to the three coordinate axes. Appropriate periodic conditions must be imposed on all the boundaries, which is an equivalent condition that each particle has counterparts in the neighbouring image cells, 8 in two-dimensional cases and 26 in three-dimensional cases.

The periodic conditions require the modification to the computations of contact and magnetic interaction of the particles. In principle, the contact search algorithm and the subsequent force calculations should include all the images of the particles. The calculation of short-ranged mechanical contact forces may include only the particle images very close to the boundaries, while the resolution of long-ranged magnetic interaction requires more particle images, but a relatively small cut-off value,  $r_c = 4R$ , given in Section 2.5.1, results in a small number of images. The actual computational domain is thus the RVE extended by the cut-off distance. Fig. 3 illustrates a two-dimensional RVE and the corresponding computational domain as well as particles with their neighbouring images.

## 6 Numerical examples

In this section, a two-stage numerical experiment will be performed to assess the applicability of the proposed approach. The simulation involves, at the first stage, the microstructure evolution of a MR fluid with four different particle concentration fractions under the action of an applied magnetic field; and at the second stage, the application of the particle chains established at the first stage as the initial configuration to investigate the rheological properties of the MR fluid under different shear loading conditions.

The MR fluid system to be considered is taken from the two-dimensional problem investigated by Ly *et al* [19]. A rectangular domain,  $0.237 \times 0.1 \text{ mm}$ , which is used as the RVE, is filled with magnetizable particles dispersed in a Newtonian fluid. The physical properties are chosen as: for the fluid, density  $\rho_f = 1000 \text{ kg/m}^3$ , dynamic viscosity  $\eta = 0.1 \text{ Pa}\cdot\text{s}$ , magnetic permeability  $\mu_f = 4\pi \times 10^{-7} \text{ N/A}^2$ ; whereas for the particles, radius  $R = 1.5 \mu\text{m}$ , density  $\rho_p = 7\rho_f$ , permeability  $\mu_p = 2000\mu_f$  (as a super-magnetic material). The applied magnetic field,  $H_0 = 1.33 \times 10^4 \text{ A/m}$ , is uniform and directed upwards.

The combined lattice Boltzmann and discrete element approach proposed in previous sections is employed, in which the magnetic forces are described by the mutual dipole model; the hydrodynamic forces are computed from the modified lattice Boltzmann equation; and the contact forces are evaluated with the Hertzian model.

### 6.1 Particle chain formation

Simulations are performed for four samples of the MR fluid with 170, 341, 682 and 1024 particles which correspond to 5, 10, 20 and 30% particle volume fractions (calculated in a 2D sense), respectively. The periodic boundary conditions are imposed on all the boundaries. The procedure is terminated when a steady-state is achieved.

The microstructure evolution of the MR fluid for the four samples are depicted in Figs. 4-7. It can be seen that under the action of the applied magnetic field, the particles aggregate and form short fragmented chains that align in the direction of the applied magnetic field. As time progresses further, these short chains merge together and form longer chains. At the same time, the spacing between these chains increases. Theoretically, the final chain structure corresponds to a minimum energy (magnetic plus elastic) state. The number and shape of the chain structure are in good agreement with those depicted in [19].

The dynamic evolution of the particles can be monitored by the history plot of the total kinetic energy of the particles. A small (near zero) value of the total kinetic energy indicates that a steady-state is reached. With this history plot, the response time of the MR fluid can also be identified.

Fig. 8 is the history plot of the total kinetic energy for the MR fluids with 10% and 30% particle volume fractions. The larger kinetic energy at the initial stage corresponds to the active motion of the particles. The local spikes represent the merging of the short chains. Compared with the 10% volume fraction curve, there are far fewer spikes in the

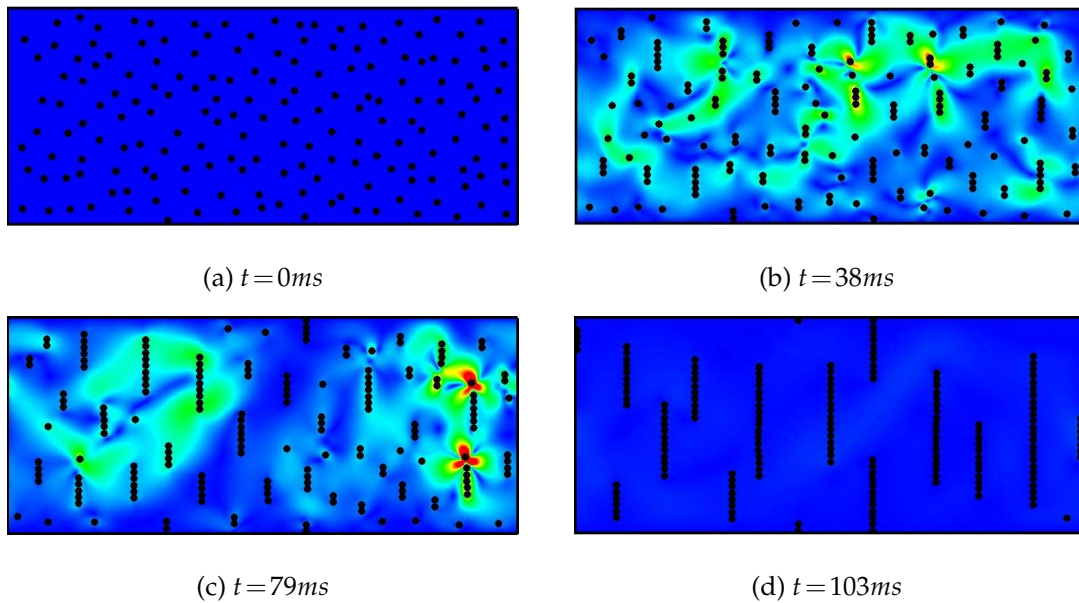


Figure 4: Microstructure evolution – total velocity contour: 5% volume fraction.

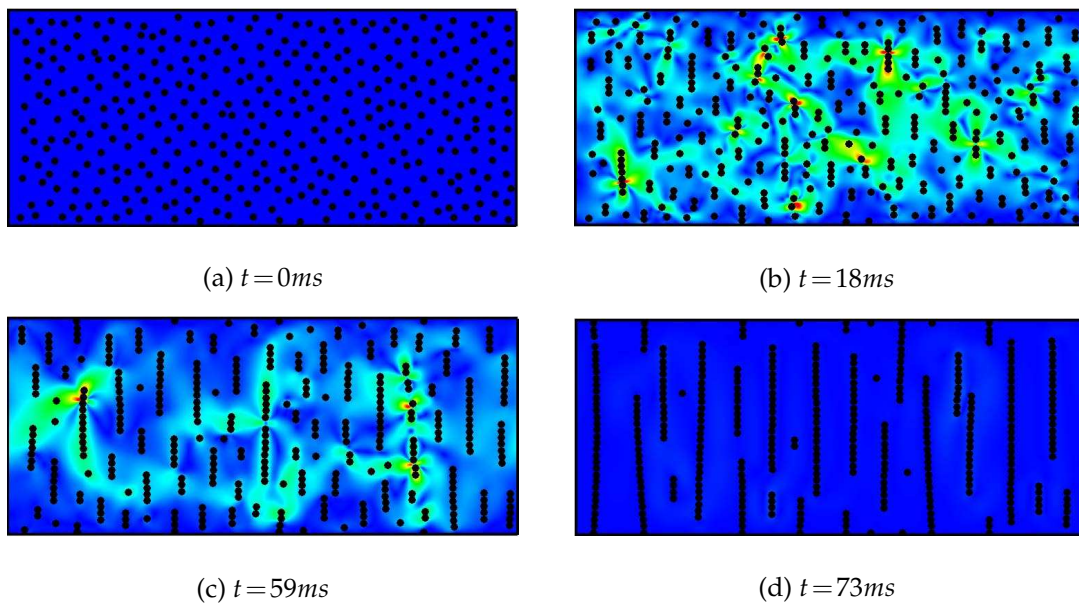


Figure 5: Microstructure evolution – total velocity contour: 10% volume fraction.

30% volume fraction case which indicates a slower particle motion since the particles generally travel shorter distances to form the chains.

The simulations have established that the times for the systems to approach a steady state are approximately inversely proportional to the particle volume fractions, which

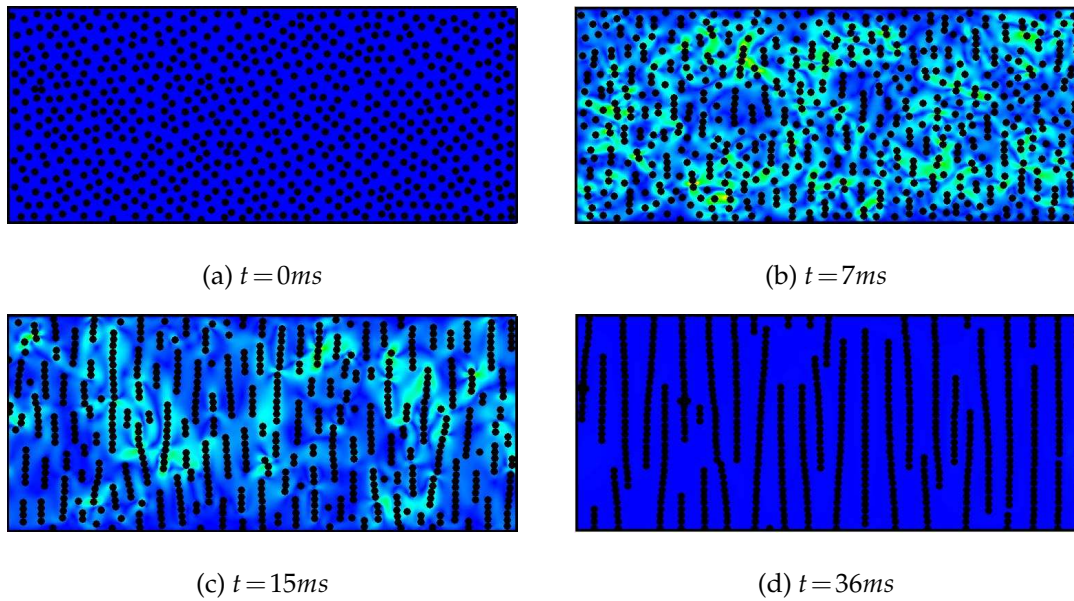


Figure 6: Microstructure evolution – total velocity contour: 20% volume fraction.

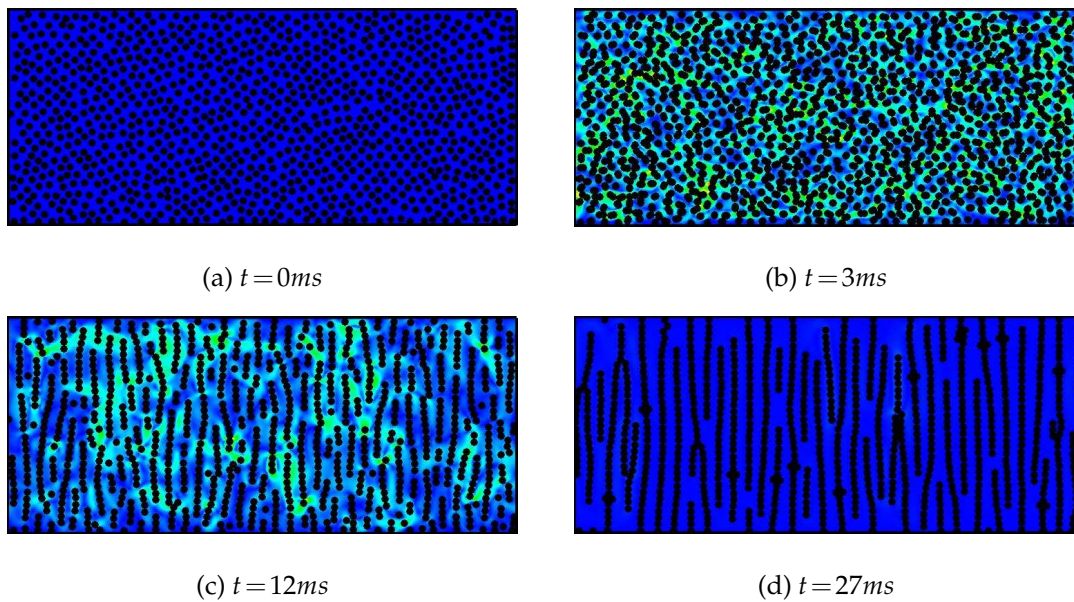


Figure 7: Microstructure evolution – total velocity contour: 30% volume fraction.

are around 103, 73, 36 and 27 milliseconds respectively for volume fractions 5, 10, 20 and 30%. Clearly the steady state is reached faster for a higher volume concentration of the particles. This observation is again in fairly good agreement with that in [19].

Simulations have also been performed for different intensities of the applied magnetic

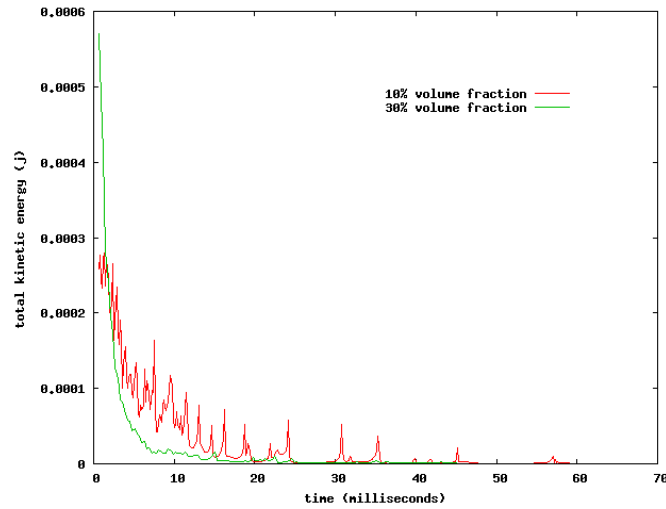


Figure 8: Kinetic energy history for MR fluids with 10% and 30% particle volume fractions.

fields  $H_0$  and different viscosities of the fluid  $\eta$ . Except that stronger magnetic field and lower fluid viscosity result in a shorter response times, the final chain configurations are not much different, implying that the particle volume fraction plays a dominant role in the particle dynamic simulation. In particular, the mutual dipole model, though inaccurate when the particles are very close, may be sufficient if only the microstructure of the particle chains is of interest.

## 6.2 Rheological property study

In the absence of an externally applied magnetic field, the viscosity of a MR fluid increases with the particle volume fraction. This is obviously due to the fact that the fluid motion is more restricted with more suspended particles.

As shown in the previous subsection, with the application of an external magnetic field, columnar particle chains are formed which are perpendicular to the direction of the fluid flow in the MR fluid. As a result, the fluid motion is largely restricted. This change in the suspension microstructure greatly alters the rheological properties of the fluid. To examine the MR effect, the following numerical tests are performed to establish the relationship between the applied shear loading and the resulting shear stress or viscosity under different magnetic field strengths.

The formulated steady-state particle chains are applied as the initial configuration of the MR fluid system. In the following simulations, the MR fluid with 10% particle volume fraction investigated in the previous subsection is chosen. The fluid domain is divided into a  $475 \times 201$  square lattice with lattice spacing  $h = 0.5 \mu\text{m}$ . The relaxation time is chosen to be  $\tau = 0.75$  which gives a time step for the fluid as  $2.08 \times 10^{-10} \text{s}$ . As the time step with a time step factor of 0.1 for the discrete element simulation is computed as  $1.67 \times 10^{-10} \text{s}$ ,

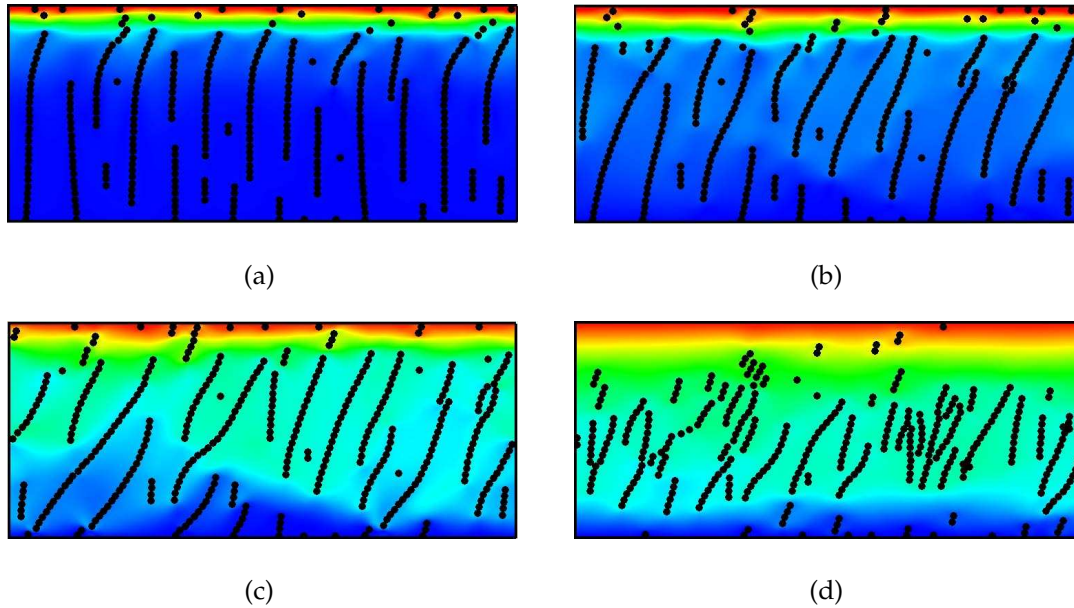


Figure 9: Four snapshots in a shear mode simulation:  $H_0 = 1.33 \times 10^4 A/m$ ,  $\dot{\gamma} = 750 s^{-1}$ .

no subcycling is required to perform in this case.

A constant horizontal velocity  $v_0$  to the right is applied to the top boundary of the problem domain, and the equivalent shear rate is  $\dot{\gamma} = v_0/W$ , with  $W = 0.1mm$  being the height of the domain. By changing the value of  $v_0$ , different shear rates can be applied. The bottom boundary is assumed to be no-slip, and the left and the right boundaries are periodic. Due to the shear loading conditions, the boundary conditions for the particles are slightly modified. The particles are restrained between the top and bottom boundaries, which is achieved by implementing mechanical contact conditions between the particles and the boundaries. For the magnetic interaction computation, however, the same full periodic conditions as those in the previous particle dynamic simulations are imposed.

During the course of the simulation, the total horizontal shear force,  $F_s$ , acting on the top boundary is recorded. The final converged value, when divided by the total length  $L = 0.237mm$  of the top boundary, gives the apparent stress  $\sigma = F_s/L$ . The apparent viscosity is then calculated as  $\sigma/\dot{\gamma}$ .

Eight different shear rates,  $\dot{\gamma} = 10, 20, 50, 100, 250, 500, 750, 1000 s^{-1}$  and three different magnetic intensities  $H = H_0, 2H_0, 0.5H_0$  which combine into 24 different cases, are simulated.

Fig. 9 depicts four snapshots of a shear mode simulation with a magnetic strength  $H_0 = 1.33 \times 10^4 A/m$  and a shear rate  $\dot{\gamma} = 750 s^{-1}$ . Under the shear operation, the particles close to the top boundary break from the chains first (Fig. 9a), then the (long) particle chains soon get deformed (Fig. 9b), detach from the bottom boundary (Fig. 9c), and finally

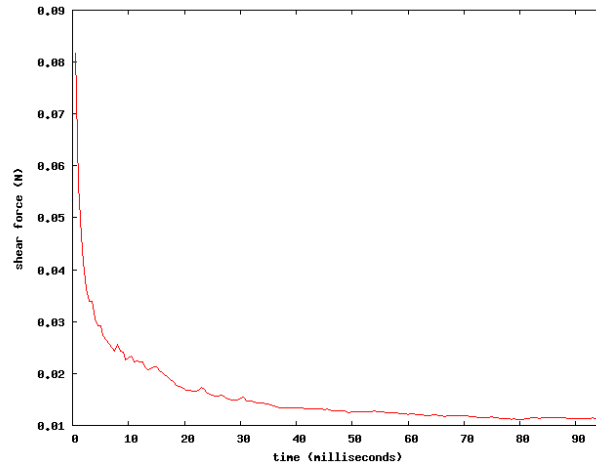


Figure 10: Shear force history in a shear mode simulation:  $H_0 = 1.33 \times 10^4 A/m$ ,  $\dot{\gamma} = 750 s^{-1}$ .

break into shorter chains (Fig. 9d), which corresponds to a sharp decrease in the shear force at the initial stage and achieves a steady-state afterwards, as shown in Fig. 10.

Fig. 11 depicts the shear stress and viscosity as a function of the applied shear rate for three different magnetic strengths. It can be seen that the MR fluid behaves like a Bingham fluid. Fig. 11(b) indicates the shear thinning behaviour of the MR fluid, whereby the viscosity upon yielding decreases with the increased shear rate. This phenomenon can be explained by the fact that with increase of the shear rate, the microstructure formed is destroyed rapidly by the increased shear stresses; longer particle chains are broken into shorter chains, which improves the fluidity of the fluid and leads to a decrease in fluid viscosity.

Fig. 11 also shows that both viscosity and shear stress increase with increase of the magnetic field strength, as expected. The magnetic interaction forces between the suspended particles increase with increase of the magnetic field strength which causes larger resistance to the fluid flow and therefore the MR fluid gains larger viscosity and shear stress. Thus, unlike the chain formation, the accuracy of the magnetic force models has a major effect on the simulated rheological properties of a MR fluid.

## 7 Concluding remarks

This paper has presented a computational procedure for numerical modelling of MR fluids, in which the particle dynamics is simulated by the discrete element method, while the fluid field is resolved with the lattice Boltzmann method. The coupling between the fluid and the particles are realized through the hydrodynamic interactions.

The magnetic force models are central to the MR fluid simulation. The fixed dipole and mutual dipole models are reviewed. A simple iterative procedure, taking advan-

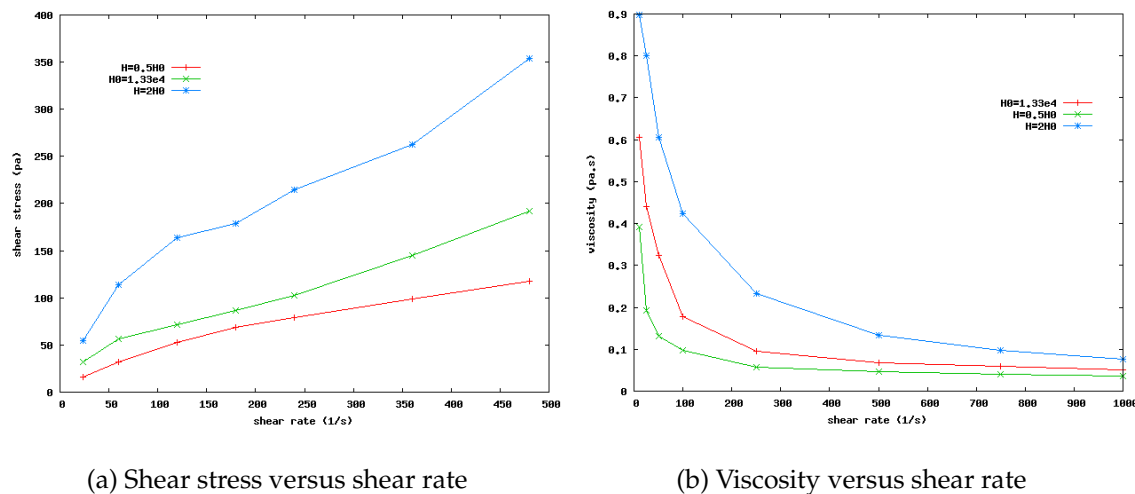


Figure 11: Correlations between shear stress/viscosity and shear rate under three different magnetic fields.

tage of small time steps used in the time integration scheme, is proposed to improve the computational efficiency of the total magnetized moments in the mutual dipole model.

A number of numerical tests have been performed to assess the applicability of the proposed solution procedure. The results show that the simulations conducted can capture the major physical features of a MR fluid. The results also reveal the fact that the steady-state particle chain structure is mainly determined by the particle volume concentration, while the rheological behaviour of a MR fluid relies on the accuracy of the magnetic force model employed, particularly when the separation distance of two particles is small. This naturally raises an issue on how the accuracy of the magnetic force models can be improved while its computational simplicity and efficiency are still retained.

## References

- [1] C. K. Aidun, Y. Lu, E.-G Ding. Direct analysis of particulate suspensions with inertia using the discrete Boltzmann equation. *Journal of Fluid Mechanics*, 373:287-311, 1998.
- [2] Ted Belytschko, Wing Kam Liu and Brian Moran. *Nonlinear finite elements for continua and structures*. John Wiley & Sons Ltd, 2000.
- [3] S. Chen, G. Doolen. Lattice Boltzmann method for fluid flows. *Annual Review of Fluid Mechanics*, 30:329-364, 1998.
- [4] H. Clercx, G. Bossis. Many-body electrostatic interactions in electrorheological fluids. *Physical Review E*, 48(4): 2721-2738, 1993.
- [5] B. K. Cook, D. R. Noble, J. R. Williams. A direct simulation method for particle-fluid systems. *International Journal for Engineering Computations*, 21(2-4):151-168, 2004.
- [6] P.A. Cundall, O.D.L. Strack. A discrete numerical model for granular assemblies. *Geotechnique*, 29:47-65, 1979.
- [7] Z.G. Feng, E. E. Michaelides. The immersed boundary-lattice Boltzmann method for solving fluid particles interaction problems. *Journal of Computational Physics*, 195:602-628, 2004.

- [8] Z. G. Feng and E. E. Michaelides. Proteus: a direct forcing method in the simulations of particulate flows. *Journal of Computational Physics*, 202:20-51, 2005.
- [9] Y. T. Feng, D. R. J. Owen. An augmented spatial digital tree algorithm for contact detection in computational mechanics. *International Journal for Numerical Methods in Engineering*, 55:556-574, 2002.
- [10] Y. T. Feng. On the central difference algorithm in discrete element modeling of impact. *International Journal for Numerical Methods in Engineering*, 64(14):1959-1980, 2005.
- [11] Y. T. Feng, K. Han, D. R. J. Owen. Coupled lattice Boltzmann method and discrete element modelling of particle transport in turbulent fluid flows: computational issues. *International Journal for Numerical Methods in Engineering*, 72 (9):1111-1134, 2007.
- [12] K. Han, D. Perić, D. R. J. Owen and J. Yu. A combined finite/discrete element simulation of shot peening process. part II: 3D interaction laws. *International Journal for Engineering Computations*, 17(6/7): 684-702, 2000.
- [13] K. Han, Y. T. Feng, D. R. J. Owen. Numerical simulations of irregular particle transport in turbulent flows using coupled LBM-DEM. *Computer Modeling in Engineering & Science*, 18(2):87-100, 2007.
- [14] Tae Gon Kang, Martien A. Hulsen, Jaap M.J. den Toonder, Patrick D. Anderson, Han E.H. Meijer. A direct simulation method for flows with suspended paramagnetic particles. *Journal of Computational Physics*, 227:4441-4458, 2008.
- [15] Eric E. Keaveny, Martin R. Maxey. Modeling the magnetic interactions between paramagnetic beads in magnetorheological fluids. *Journal of Computational Physics*, 227:9554-9571, 2008.
- [16] D. Klingenberg, F. van Swol, C. Zukoski. The small shear rate response of electrorheological suspensions. I. Simulation in the point-dipole limit. *Journal of Chemical Physics*, 94(9):6160-6169, 1991.
- [17] D. Klingenberg, F. van Swol, C. Zukoski. The small shear rate response of electrorheological suspensions. II. Extension beyond the point-dipole limit. *Journal of Chemical Physics*, 94(9):6170-6178, 1991.
- [18] A. Ladd. Numerical simulations of fluid particulate suspensions via a discretized Boltzmann equation (Parts I & II). *Journal of Fluid Mechanics*, 271:285-339, 1994.
- [19] H. V. Ly, F. Reitich, M. R. Jolly, H. T. Banks, K. Ito. Simulations of particle dynamics in magnetorheological fluids. *Journal of Computational Physics*, 155:160-177, 1999.
- [20] D. Noble, J. Torczynski. A lattice Boltzmann method for partially saturated cells. *International Journal of Modern Physics C*, 9:1189-1201, 1998.
- [21] A.G. Olabi, A. Grunwald. Design and application of magneto-rheological fluid. *Materials and Design*, 28:2658-2664, 2007.
- [22] D. Qi, L. Luo. Rotational and orientational behaviour of three-dimensional spheroidal particles in Couette flows. *Journal of Fluid Mechanics*, 477:210-213, 2003.
- [23] J. Rabinow. The magnetic fluid clutch. *AIEE Transactions*, 67:1308, 1948.
- [24] J. A. Stratton. *Electromagnetic Theory (First Edition)*. McGraw-Hill, 1941.